



Jetting Phenomenon in Cold Spray: A Critical Review on Finite Element Simulations

S. Rahmati¹ · J. Mostaghimi¹ · T. Coyle¹ · A. Dolatabadi¹

Submitted: 14 December 2023 / in revised form: 28 February 2024 / Accepted: 20 March 2024 / Published online: 15 April 2024
© ASM International 2024

Abstract This paper offers a concise critical review of finite element studies of the jetting phenomenon in cold spray (CS). CS is a deposition technique wherein solid particles impact a substrate at high velocities, inducing severe plastic deformation and material deposition. These high-velocity particle impacts lead to the ejection of material in a jet-like shape at the periphery of the particle/substrate interface, a phenomenon known as “jetting”. Jetting has been the subject of numerous studies over recent decades and remains a point of debate. Two main mechanisms, Adiabatic Shear Instability (ASI) and Hydrodynamic Pressure-Release (HPR), have been proposed to explain the jetting phenomenon. These mechanisms are mainly elucidated through finite element method (FEM) simulations, a numerical technique rooted in continuum mechanics. However, it is important to emphasize that FEM is limited by the equations established for analysis, and as such, its predictive capabilities are confined to those principles clearly defined within these equations. The choice of employed equations and approaches significantly influence the outcomes and predictions in FEM. While recognizing FEM’s capabilities, this study reviews the ASI and HPR mechanisms within the context of CS. Additionally, this paper reviews FEM’s algorithms and the core principles that govern FEM in calculating plastic deformation, which can lead to the formation of jetting.

Keywords cold spray · finite elements method · jetting

Introduction

Cold Spray (CS) is a deposition process in which solid particles adhere to a substrate after impacting at high velocities. In this process, the particles’ temperature is lower than their melting point prior their impact, resulting severe plastic deformation at extremely high strain rates up to 10^9 s^{-1} (Ref 1). It has been shown that upon impact of a solid particle at high velocities, a jet-shape material ejection occurs at the periphery of the particle/substrate interface called “jetting” (Ref 2, 3), as illustrated in Fig. 1. The jetting phenomenon can occur in three cases, i.e., only for the particle (Fig. 1a, Ref 4), only for the substrate (Fig. 1b, Ref 5), and simultaneously for the particle and the substrate (Fig. 1c, Ref 6). The formation of jetting depends on several factors such as material properties, material temperature, particle size, and the impact velocity.

The phenomenon of jetting has been the topic of numerous works over the last decades and is still a point of contention (Ref 7-9). Adiabatic Shear Instability (ASI) (Ref 6) and Hydrodynamic Pressure-Release (HPR) (Ref 7) have been proposed as the main mechanisms for the occurrence of jetting in CS.

Both the “ASI” and “HPR” mechanisms have been proposed based on Finite Element Method (FEM) simulations, which are based on continuum mechanics. Fundamentally, FEM serves as a numerical technique aimed at resolving the constitutive equations governing phenomena observed in the natural world. It is important to note that FEM, in itself, does not unveil novel physical insights or mechanisms; rather, the outcomes it produces are intricately tied to the equations employed in the analysis. For instance, in Ref 10, the significance of flow stress models in FEM simulations of CS became evident. By simulating the impact of a single copper particle onto a copper

✉ S. Rahmati
saeed.rahmati@utoronto.ca

¹ Centre for Advanced Coating Technologies, University of Toronto, Toronto, ON, Canada

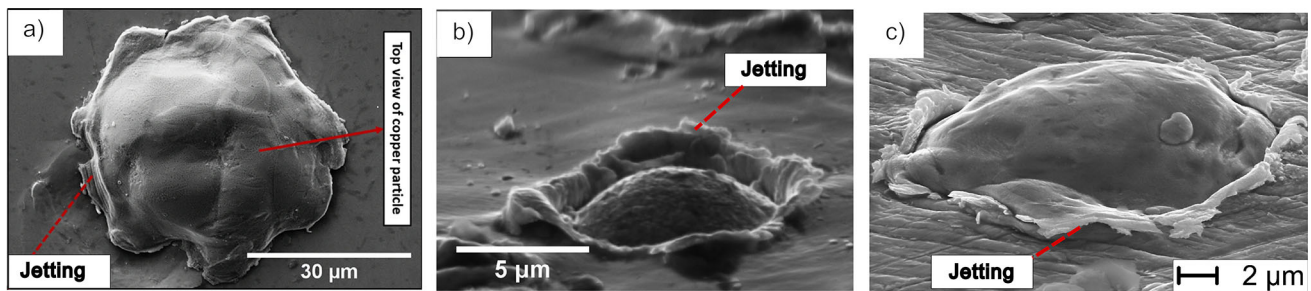


Fig. 1 Scanning Electron Microscopic (SEM) images of deposited CS's particles displaying the jetting phenomenon for: (a) Particle (Ref 4), (b) Substrate (Ref 5), and (c) For both particle and substrate (Ref 6). (a) Copper on low-carbon steel (Ref 4), (b) CrMnCoFeNi alloy powder on nickel substrate (Ref 5), and (c) Copper particle on copper substrate (Ref 6). Ref 4 Bonding Mechanisms in Cold Spray: Influence of Surface Oxidation During Powder Storage, Maryam Razavipour et al. *Journal of Thermal Spray Technology*, Springer Nature, 2020, reproduced with permission from SNCSC. Ref 5

Reprinted from *Surface and Coatings Technology*, Vol. 425, Roghayeh Nikbakht, Mohammad Saadati, Taek-Soo Kim, Mohammad Jahazi, Hyoung Seop Kim, Bertrand Jodoin, Cold spray deposition characteristic and bonding of CrMnCoFeNi high entropy alloy, p. 127748, Copyright 2021, with permission from Elsevier. Ref 6 *Acta Materialia*, Vol. 51, Hamid Assadi, Frank Gärtner, Thorsten Stoltenhoff, Heinrich Kreye, Bonding mechanism in cold gas spraying, p. 4379-4394, Copyright 2003, with permission from Elsevier

substrate, using six distinct constitutive equations appropriate for high strain rate plasticity, it became clear that these flow stress models have a notable influence on the anticipated deformations and mechanical responses. Notably, the Johnson-Cook (JC) model (Ref 11) yielded predictions of substantial material jetting, while the Gao-Zhang model (Ref 12) indicated the absence of jetting at the same impact velocity.

However, both the “ASI” and “HPR” mechanisms have found their place as benchmarks in various studies. While FEM is a valuable and indispensable tool in engineering and materials science, it is important to acknowledge its inherent limitations when it comes to generating entirely new physical insights. Nonetheless, FEM provides a powerful means to simulate and analyze complex phenomena. In the case of this study, FEM plays a crucial role in revealing the material behavior and the occurrence of jetting in high velocity impacts. To bridge the knowledge gap, this research aims to present a concise and critical review of the proposed mechanisms for jetting within the CS context, alongside relevant literature. Furthermore, by highlighting the fundamental principles that underlie FEM simulations, this work seeks to clarify how FEM predicts and explains the formation of jetting during high-velocity impacts.

Adiabatic Shear Instability

The ASI mechanism occurs when thermal softening dominates over the work hardening effects due to the localization of plastic deformation (Ref 13). The shear localization leads to an increase in material temperature locally, resulting in a decrease in flow stress. This local reduction in flow stress causes further strain localization

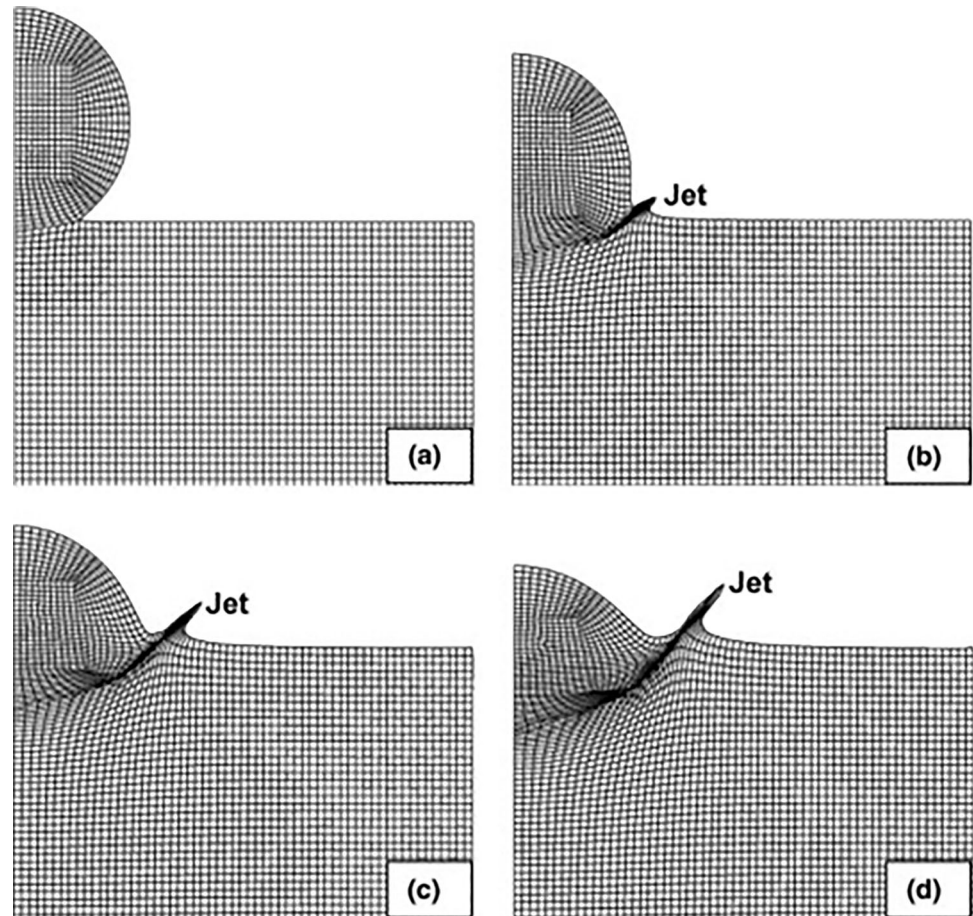
and, consequently, generates more heat. Eventually, this sequence of events leads to an instability in the material, resulting in a fluid-like behavior of the material while it remains in the solid state.

The ASI mechanism was introduced to the field of CS by Assadi et al. (Ref 6). They simulated the impact of a single copper particle with different velocities on a copper substrate using a Lagrangian approach (Ref 14). For particles exhibiting jetting behavior, they observed a rapid change in strain, temperature, and stress for an element at the particle surface, which experienced the highest amount of deformation within the particle. They then proposed that this abrupt change signifies the transition from plastic flow to viscous flow, showing the occurrence of ASI. Consequently, Assadi et al. (Ref 6) proposed that the predicted jet in FEM simulations arises from the ASI mechanism. Building upon this hypothesis, Grujicic et al. (Ref 15) and Bae et al. (Ref 16) further extended the research in their respective studies, both utilizing a Lagrangian approach.

Figure 2, Ref 15 illustrates the simulation results, depicting the deformation evolution of both the particle and the substrate, using the Lagrangian approach. Grujicic et al. (Ref 15) employed these results as an indicator of jetting and the occurrence of ASI during the impact process. They also plotted the history of strain, temperature, strain rate, and stress for various velocities, revealing a sudden change in all these variables at the velocity corresponding to the onset of ASI, as shown in Fig. 3, Ref 15. The utilization of a sudden drop in stress and/or changes in strain or temperature has also been documented in several other studies (Ref 16-22), which further build upon the foundational work of Assadi et al. (Ref 6).

Li et al. (Ref 23, 24) were the first (Ref 25) to highlight that the abrupt change in plastic strain obtained from the Lagrangian approach can be attributed to abnormal element

Fig. 2 Deformation evolution of the particle and the substrate during the particle impact on the substrate. Material contact time: (a) 4.4 ns; (b) 13.2 ns; (c) 22.0 ns and (d) 30.8 ns (Ref 15). Reprinted from *Materials & Design*, Vol. 25, M. Grujicic, C.L. Zhao, W.S. DeRosset, D. Helfritsch, Adiabatic shear instability based mechanism for particles/substrate bonding in the cold-gas dynamic-spray process, p. 681-688, Copyright 2004, with permission from Elsevier



deformations and should not be directly correlated with the actual occurrence of ASI during particle impact. They demonstrated that by employing the Arbitrary Lagrangian Eulerian (ALE) method (Ref 14), issues linked to severe mesh distortion can be mitigated. Later, the pioneering work of Li et al. (Ref 23, 24, 26) received further support from Yu et al. (Ref 27), who employed the Eulerian approach (Ref 14) to address the challenge of element distortion. Their findings disclosed the presence of notable material jetting at high velocities, without exhibiting sudden variations in strain, as displayed in Fig. 4, Ref 27.

In numerical simulations, especially in the context of a Lagrangian approach, mesh distortion is a critical factor that can significantly impact the accuracy of the results. Yildirim et al. (Ref 28) compared three different simulation approaches and found that, at relatively high velocities, the pure Lagrangian approach leads to significant distortion in elements, resulting in inaccurate deformation prediction. Mesh distortion occurs when the elements, such as quadrilaterals in two-dimensional simulations or hexahedra in three-dimensional simulations, deviate from their ideal shape due to geometric deformation, excessive stretching,

skewing, warping, twisting and in extreme cases, may even lead to non-physical negative volumes (Ref 29, 30). The extent of distortion and its influence on result accuracy can vary (Ref 29). Some cases exhibit minor errors, while others may introduce substantial discrepancies.

While the FEM/Explicit solver is more resilient in handling some degree of distortion compared to FEM/Implicit, it remains essential for the user to prioritize maintaining good mesh quality and validate the obtained results. This resilience in handling distorted elements is primarily attributed to the explicit time integration techniques that do not require solving a system of equations at each time step (Ref 31, 32).

As previously mentioned, foundational studies (Ref 6, 15, 16) on the ASI in CS involved FEM simulations in a Lagrangian scheme. As illustrated in Fig. 2, it is apparent that elements located at the periphery of the particle/substrate zone experienced significant distortion due to the pronounced deformation within this region. This severe distortion is attributed to warping and excessive stretching, ultimately resulting in non-physical negative volume issues for several elements in the jetting region. As a result, data obtained from these severely distorted elements proved to

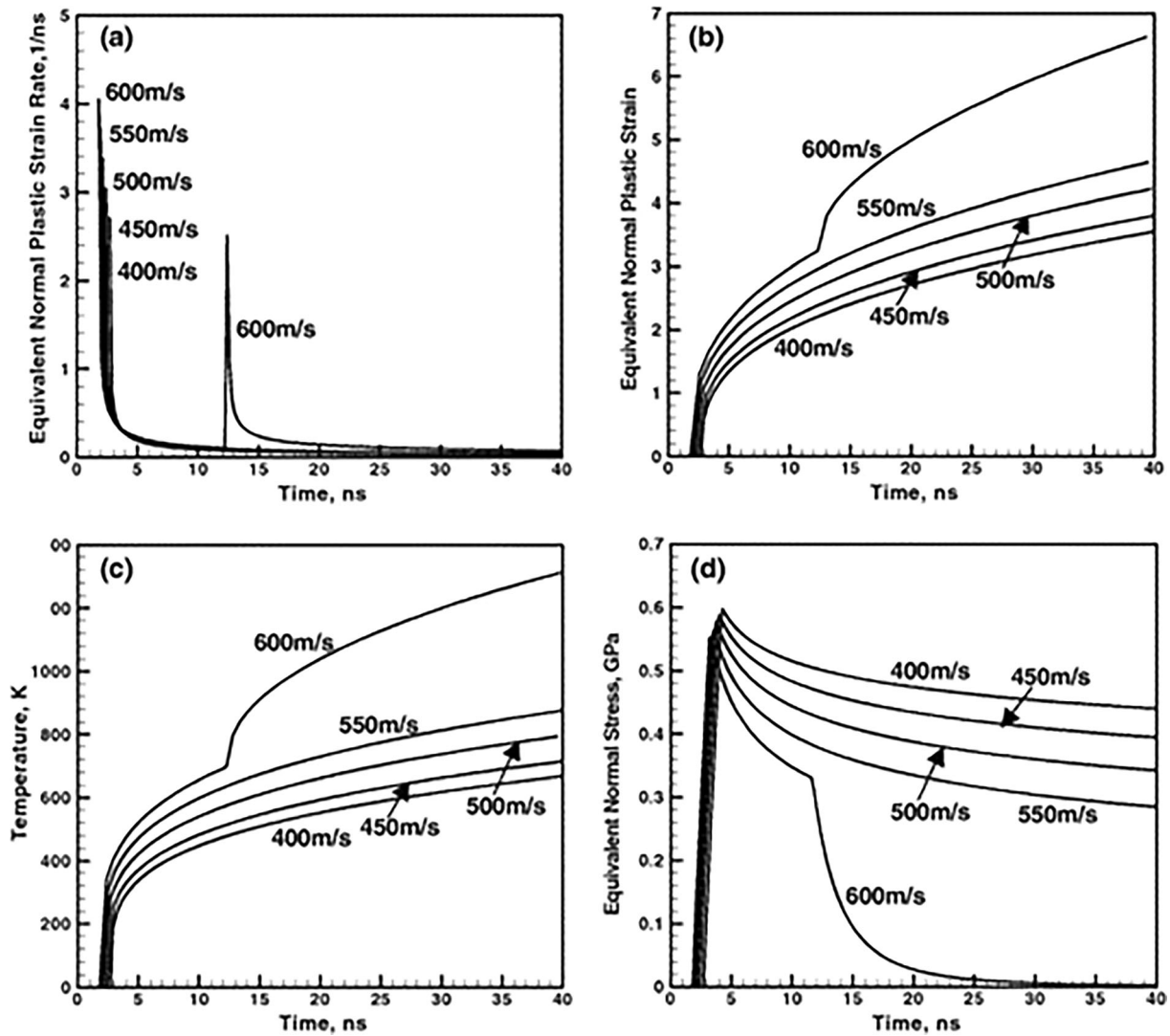


Fig. 3 The history of (a) the equivalent plastic strain rate; (b) the equivalent plastic strain; (c) the temperature; and (d) the equivalent normal stress for an element located at the copper/particle surface. These evolutions occur as a result of the particle impacting on a copper substrate, with different initial impact velocities (Ref 15).

be unreliable. Consequently, the abrupt changes in stress, temperature, strain, and strain rate (depicted in Fig. 3) cannot be used as ASI indicators.

Hydrodynamic Pressure Release

Adiabatic Shear Bands are typically associated with ASI occurrence. However, Hassani-Gangaraj et al. (Ref 7) reported that the absence of adiabatic shear bands in the deposited particles suggests that ASI is not the cause of the observed material jetting in CS. They proposed an alternative explanation, suggesting that jetting results from strong shock waves interacting with the expanding edge of

Reprinted from Materials & Design, Vol. 25, M. Grujcic, C.L. Zhao, W.S. DeRosset, D. Helfritsch, Adiabatic shear instability based mechanism for particles/substrate bonding in the cold-gas dynamic-spray process, p. 681-688, Copyright 2004, with permission from Elsevier

the particle and forms due to hydrodynamic plasticity, see Fig. 5 (Ref 7). This newly proposed mechanism was termed “Hydrodynamic Pressure Release (HPR)”. They argued that jetting occurs due to the release of highly localized tension (up to five times the material strength) at the particle’s edge. This tension emerges from the interaction of pressure waves and the free surface at the edge of contact. The release of this tension further accelerates material, leading to jetting.

To substantiate their argument, Hassani-Gangaraj et al. (Ref 7) conducted simulations involving the impact of a 10 μm particle onto a copper substrate using the JC constitutive material model. The flow stress in the JC model is defined as follows:

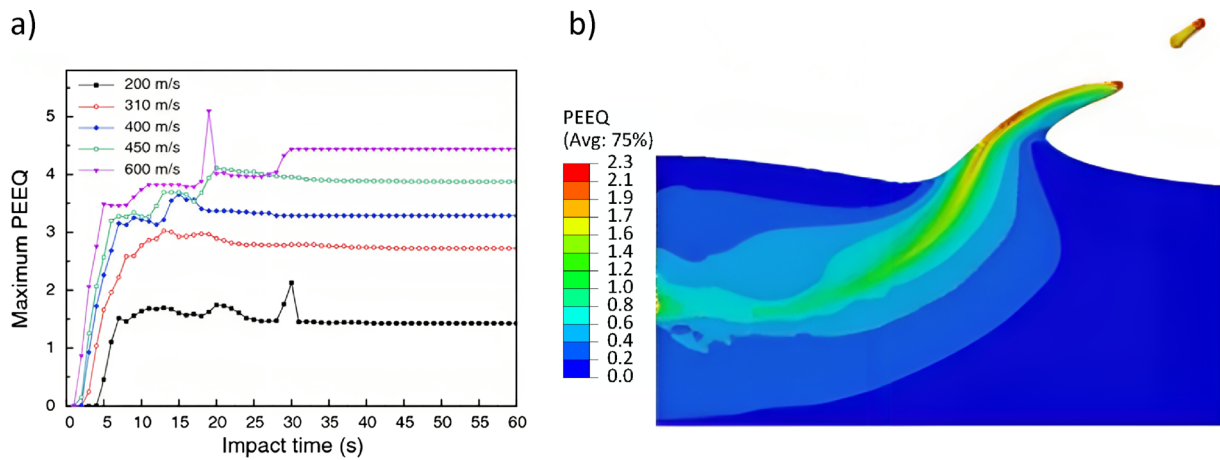


Fig. 4 (a) Evolution of equivalent plastic strain of a 20 μm copper particle on a copper substrate at different velocities, (b) Distribution of the equivalent plastic strain on the particle and the substrate after the impact at 600 m/s (Ref 27). Finite Element Simulation of

Impacting Behavior of Particles in Cold Spraying by Eulerian Approach, Yu et al. Journal of Thermal Spray Technology, Springer, 2011, reproduced with permission from SNCSC

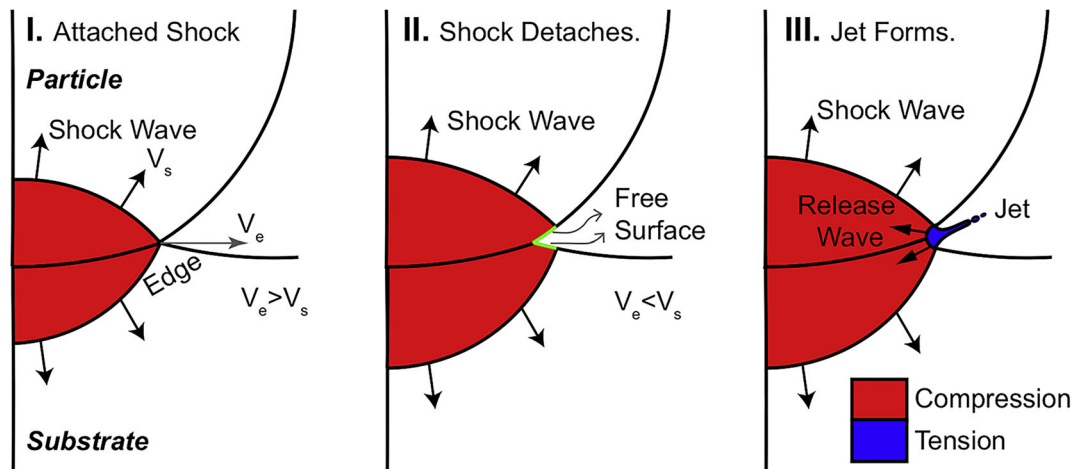


Fig. 5 Schematic representing the initiation of jetting in CS: Stage I. Impact generates a shock wave. Stage II. Shock wave separates from the leading edge. Stage III. Formation of jetting based on pressure releases (Ref 7). Reprinted from Acta Materialia, Vol. 158, Mostafa

Hassani-Gangaraj, David Veysset, Victor K. Champagne, Keith A. Nelson, Christopher A. Schuh, Adiabatic shear instability is not necessary for adhesion in cold spray, p. 430-439, Copyright 2018, with permission from Elsevier

$$\sigma = \left(A + B\varepsilon_p^n \right) \left(1 + C \ln \frac{\dot{\varepsilon}_p}{\dot{\varepsilon}_0} \right) \left(1 - \left[\frac{T - T_r}{T_m - T_r} \right]^m \right) \tag{Eq 1}$$

where A , B , n , C , and m are material constant. ε_p , and $\dot{\varepsilon}_p$ are the equivalent plastic strain and equivalent plastic strain rate, respectively. $\dot{\varepsilon}_0$ is the strain rate at which material constants are obtained, called the reference strain rate. T is the material temperature. T_r and T_m are respectively the reference temperature and the melting temperature of the material. As shown in Eq 1, the JC model is composed of three bracketed terms. The first bracket represents strain hardening, the second computes strain rate hardening, and the third term takes into account the thermal softening effect.

In (Ref 7), impact simulations were performed after excluding the thermal softening component of the JC model (the third bracket in Eq 1). The outcomes of simulations revealed that significant material jetting still occurs as a result, see Fig. 6. This led to the conclusion that thermal softening, and consequently the ASI mechanism, is not an essential requirement for jetting to occur. Notably, in this simulations, the Coupled Eulerian-Lagrangian (CEL) (Ref 14) method was employed to circumvent any mesh distortion associated with the conventional Lagrangian approach, which is commendable.

However, a recent study by Pereira et al. (Ref 33) presents findings that contradict the conclusions of (Ref 7). Pereira et al. (Ref 33) elucidated the jetting mechanisms involved in the high-velocity impact of copper particles

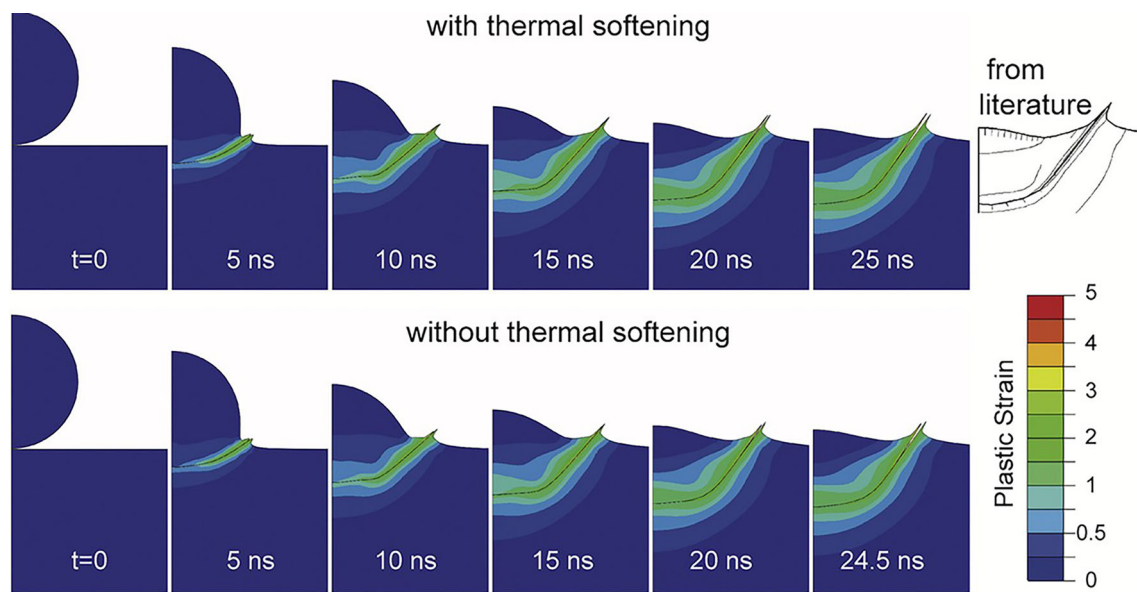


Fig. 6 Plastic strain distribution and snapshots of deformation during the impact with and without the thermal softening effects (Ref 7). Reprinted from *Acta Materialia*, Vol. 158, Mostafa Hassani-Gangaraj, David Veysset, Victor K. Champagne, Keith A. Nelson, Christopher

A. Schuh, *Adiabatic shear instability is not necessary for adhesion in cold spray*, p. 430-439, Copyright 2018, with permission from Elsevier

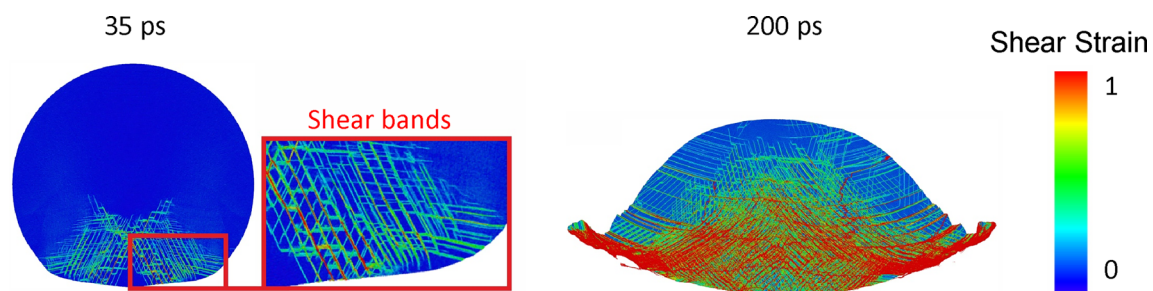


Fig. 7 Snapshots of atomic shear strain distributions for a 0.2 μm copper particle after impacting a copper substrate at 700 m/s, illustrating the accumulation of shear bands structures in the jetting zone (Ref 33). Reprinted from *Additive Manufacturing*, Vol. 75, LM

Pereira, A. Zúñiga, B. Jodoin, RGA Veiga, S. Rahmati, *Unraveling jetting mechanisms in high-velocity impact of copper particles using molecular dynamics simulations*, p. 103755, Copyright 2023, with permission from Elsevier

using Molecular Dynamics (MD) simulations. They indicated that the amplitude of the tensile waves reflected from the free surfaces is inadequate to drive the material state from compression to tension during impact. Consequently, these waves did not exert a direct influence on the generation of jetting in CS. Instead, the results pointed to shear localization as the primary factor contributing to jetting formation, as depicted in Fig. 7 (Ref 33).

The results showed a mechanism similar to ASI to be responsible for the occurrence of jetting in CS. However, further investigation is required to draw a conclusive comparison. Nevertheless, one significant conclusion that can be drawn from this study is that jetting in CS results from the accumulation of dislocations and interactions

between them, and it is not related to hydrodynamic plasticity (Ref 33).

Furthermore, it is important to note that while both ASI (Ref 6, 15, 16) and HPR (Ref 7) mechanisms suggest jetting as a sudden phenomenon, Pereira et al. (Ref 33) demonstrated that jetting occurs progressively. In this scenario, instability doesn't manifest suddenly; instead, the temperature gradually increases, ultimately leading to a fluid-like behavior (instability) in the jetting zone.

These findings raised a question: If shear localization (which leads to softening) is the driving mechanism of jetting, how can FEM predict jetting while excluding the thermal softening effect? In the following section, we will address this question by reviewing the procedure and

formulas used by FEM to calculate jetting, or more precisely, plastic deformation.

Review of FEM Principles for Plastic Deformation (A Cuboid Impact Case Study)

The primary aim of this section is to review the fundamental approach employed by FEM for calculating plastic deformation. To achieve this, all explanations and equations will be presented based on a simple Lagrangian method utilizing two-dimensional (2D) (quadrilaterals) elements as a case study. This presentation assumes the material’s behavior to be linearly elastic and follow the von Mises criterion for plasticity. It is worth noting that diverse methods have been proposed to computationally model plastic behavior. Here, a brief explanation of one such method will be provided as an example, bearing in mind that these methods generally share a similar approach, differing primarily in specific equations. A comprehensive exploration of all FEM details exceeds the scope of this work. Interested readers are directed to (Ref 14, 34-36) for an in-depth description of the equations employed in FEM.

The Lagrangian approach is a conventional method for calculating deformations in solid mechanics. In a Lagrangian analysis, nodes are affixed to the material, causing Lagrangian elements to deform in accordance with the material’s deformation. As a result, element distortion can occur during simulations of substantial plastic deformation. To address this limitation, alternative approaches such as Eulerian, CEL, ALE, and Smoothed Particle Hydrodynamics (SPH) have been proposed, allowing materials to deform extensively without encountering distortion problems (Ref 14).

However, across all these advanced methods, the computation of material deformation remains rooted in the traditional Lagrangian method. For example, even in SPH, which belong to the meshless family, the approach remains fully Lagrangian (Ref 14). Similarly, in Eulerian and CEL methods, all nodes are initially assumed to be temporarily fixed with the material (in a Lagrangian phase) at the start of each time increment, with subsequent deformation occurring alongside the material. This formulation is referred to as the “Lagrange-plus-remap” scheme (Ref 14). Following this, material deformation is then transported back to the Eulerian phase.

In the context of CS, the Explicit approach, exemplified by software like ABAQUS/Explicit (Ref 14) or LS-Dyna (Ref 37), is commonly favored over Implicit analysis. This preference arises due to the ability of the explicit method to swiftly solve highly dynamic processes. In this approach, time is discretized into finite steps, denoted as Δt (the time increment). The term ‘explicit’ signifies that the state at the

end of each increment is determined solely by the displacements, velocities, and accelerations at the beginning of the increment.

To facilitate a clearer understanding of the FEM calculations related to plastic deformation, which may contribute to the formation of jetting, a simple impact simulation was conducted. Specifically, a 50 μm cuboid impacting a rigid wall at 500 m/s was modeled within a 2D plane strain system using a Lagrangian Four-node plane strain element with reduced integration points (detailed in Appendix A).

Snapshots illustrating the deformation process of the cuboid at 1.5, 10, 25, and 50 ns after the impact are presented in Fig. 8. It is evident that the formation of jetting began during the early stages of deformation, as depicted in Fig. 8(a). As the deformation progressed, the development and intensification of jetting also continued, becoming more pronounced along the cuboid’s edges. Notably, the zoomed-in views of the jetting regions within this figure reveal that the jetting occurred without causing significant element distortion.

The algorithm in FEM/Explicit at the step time t can be divided into three sequential steps (Ref 14): Step (1) Nodal calculations; Step (2) Element calculations; and Step (3) Update the time to $t + \Delta t$ and return to Step 1. Steps 1 and 2 will be elaborated in more detail in the subsequent explanations.

Step 1:

At the beginning of each increment, t , the program calculates the nodal accelerations, $\ddot{\mathbf{u}}$, by solving the dynamic equilibrium equation:

$$\ddot{\mathbf{u}}|_t = \mathbf{M}^{-1} \cdot (\mathbf{F} - \mathbf{V})|_t \tag{Eq 2}$$

where \mathbf{M} is the nodal mass matrix, \mathbf{F} is the applied external forces, and \mathbf{V} is the internal element forces.

Then, the nodal velocity is determined under the assumption of constant acceleration. According to the central difference rule (Ref 34), the velocity at the midpoint of the current increment is computed as the sum of the velocity at the midpoint of the previous increment and the change in velocity:

$$\dot{\mathbf{u}}|_{t+\frac{\Delta t}{2}} = \dot{\mathbf{u}}|_{t-\frac{\Delta t}{2}} + \frac{(\Delta t|_{t+\Delta t} + \Delta t|_t)}{2} \ddot{\mathbf{u}}|_t \tag{Eq 3}$$

Following this, the nodal displacement at the end of the increment is determined by explicitly integrating velocities over time and adding the result to the nodal displacement at the beginning of the increment:

$$\mathbf{u}|_{t+\Delta t} = \mathbf{u}|_t + \dot{\mathbf{u}}|_{t+\frac{\Delta t}{2}} \Delta t|_{t+\Delta t} \tag{Eq 4}$$

By the end of Step 1, calculations for nodal acceleration, nodal velocity, and nodal displacement are completed.

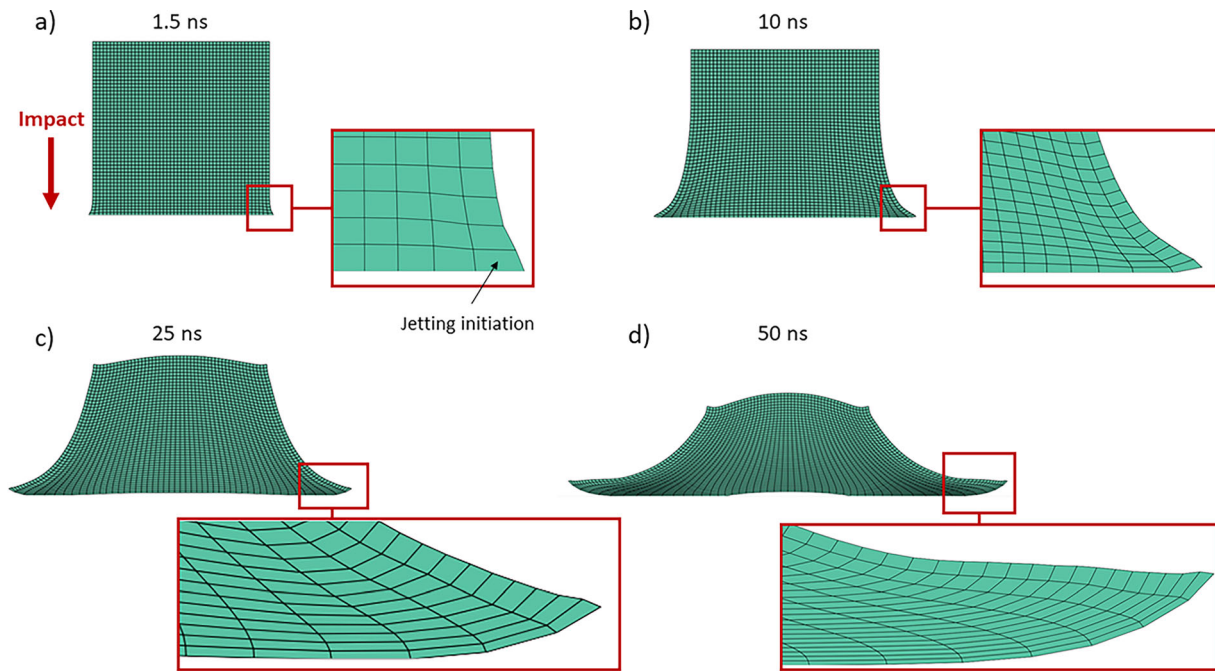


Fig. 8 Deformation process of a 50 μm copper cuboid impacting a rigid wall at 500 m/s. Snapshots taken at (a) 1.5 ns, (b) 10 ns, (c) 25 ns, and (d) 50 ns

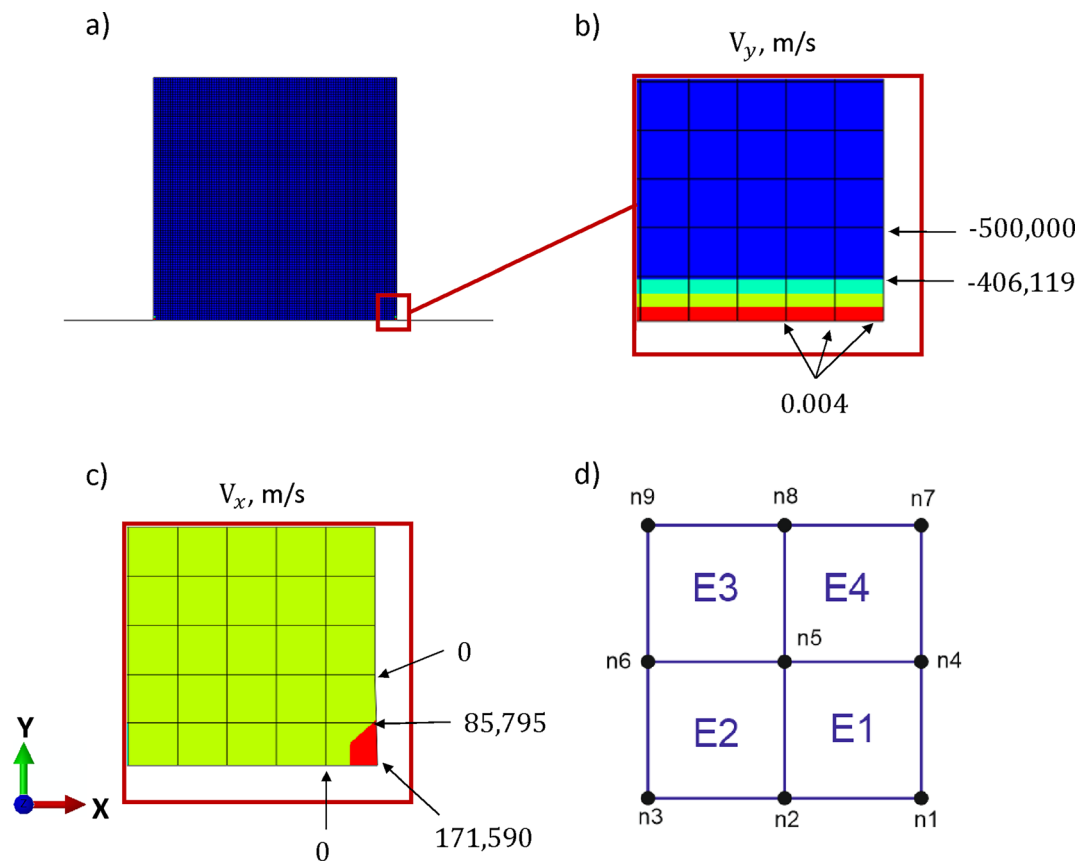


Fig. 9 (a) Cuboid at the end of the first time increment, which is 0.15 ns. (b) Enlargement showing the distribution of nodal velocity in the y -direction. (c) Enlargement showing the distribution of nodal

velocity in the x -direction. (d) Schematic representation of four elements positioned at the tip of the cuboid's edge

The distribution of nodal velocity on the cuboid at the conclusion of the first increment (0.15 ns) is depicted in Fig. 9, alongside a schematic representation of four elements located at the right edge of the cuboid. The initial element at the cuboid’s edge, E_1 , comprises four nodes— $n_1, n_2, n_4,$ and n_5 (Fig. 9d). The second element in the first layer, E_2 , similarly comprises four nodes— $n_2, n_3, n_5,$ and n_6 —where n_2 and n_5 are common with E_1 . Before impact, all cuboid nodes have a downward velocity of 500 m/s (opposite to the y direction). Figure 9(b) illustrates that nodes within each layer possess the same y -direction velocity. Nodes in the first layer, which hits the rigid wall directly (e.g., $n_1, n_2,$ and n_3), almost come to a halt. The second layer maintains a velocity of 406 m/s, while the third layer maintains a constant 500 m/s.

Before deformation starts (upon impact), each layer of nodes experiences identical internal and external forces along the y direction. Consequently, the calculated velocity remains consistent across nodes within each layer. However, a variation in the distribution of nodal velocity in the x direction is observed, see Fig. 9(c). Nodes like n_1 and n_4 encounter no restrictions in their rightward movement, whereas nodes $n_2, n_3, n_5,$ and n_6 face neighboring nodes ahead, limiting their movement in the x direction. Consequently, the maximum nodal velocity in the x direction is allocated to n_1 , as shown in Fig. 9(c).

Step 2:

Upon calculating all nodal displacements and velocities, the velocity gradient matrix, L , is computed as:

$$L = \frac{dv}{dx} \tag{Eq 5}$$

where dv is the velocity difference between two neighboring material points (or nodes) in the current configuration, x . According to continuum mechanics (Ref 34), the velocity gradient can be divided (or decomposed) into a symmetric strain rate matrix, D , and an antisymmetric rotation rate matrix, W . The decomposition allows to separate the part of the velocity gradient which causes the stretch/shear from the part which only causes the pure rotation. D is also called as the rate of deformation matrix and can be expressed as:

$$D = D^{el} + D^{pl} \tag{Eq 6}$$

where D^{el} and D^{pl} are elastic and plastic parts of the rate of deformation matrix, respectively. The Eq 6 is so-called as “additive rate of deformation decomposition”. In Abaqus (Ref 14), the rate of deformation decomposition is defined as:

$$\dot{\epsilon} = \dot{\epsilon}^{el} + \dot{\epsilon}^{pl} \tag{Eq 7}$$

where $\dot{\epsilon}^{el}$ and $\dot{\epsilon}^{pl}$ are the elastic and plastic part of strain rate tensor, $\dot{\epsilon}$, respectively.

The gradient of strain rate components of the cuboid at 0.3 ns (end of the second increment) is illustrated in Fig. 10. At 0.3 ns, only the first two layers of elements at the bottom of the cuboid have been influenced by the impact. As depicted in Fig. 10(b), the first layer of elements, which collided with the rigid wall, exhibits the maximum normal strain rate in the y direction, while the second layer’s strain rate is approximately half of that of the first layer. Similar to the findings in Fig. 9, all elements within each layer exhibit similar strain rates. The distribution of normal strain rate in the x direction is presented in Fig. 10(c). It’s evident that the first layer’s edge element holds the maximum strain rate value ($5.256 \times 10^8 \text{ s}^{-1}$), which decreases to 360.4 s^{-1} for the second element and -360 s^{-1} for the third element. The distribution of shear strain rate, shown in Fig. 10(d), also demonstrates the maximum value within the same edge element of the cuboid. Therefore, it is evident that the maximum strain rate experienced by the edge element is solely determined by the boundary conditions applied to this element, rather than the employed flow stress model.

After calculating the $\dot{\epsilon}$, the increment in total strain tensor, $d\epsilon$, is defined as the integration of strain rate tensor through time:

$$d\epsilon = \int_t^{t+\Delta t} \dot{\epsilon} dt \tag{Eq 8}$$

As a result, the total strain tensor is initially determined from the velocity gradient matrix, independent of the employed constitutive material model such as the JC model. This reveals that up to this point, the total nodal displacement and element strain along their respective directions are computed without a direct reliance on the employed flow stress model (like the JC model). Consequently, it can be concluded that the total deformation (encompassing both elastic and plastic components) remains unaffected by the flow stress model. In the following, the explanation will clarify how the flow stress model exclusively influences the plastic components of strain and stress tensors.

The increment in stress tensor, $d\sigma$, is defined based on Hook’s law (Ref 34, 38) in multiaxial form (in terms of tensor) as:

$$d\sigma = C d\epsilon^{el} = C(d\epsilon - d\epsilon^{pl}) \tag{Eq 9}$$

where C is the elastic stiffness matrix, while $d\epsilon^{el}$, and $d\epsilon^{pl}$ represent the increments in elastic and plastic strain, respectively. As a result, the stress at the end of the increment time, $t + \Delta t$, is defined as following:

$$\sigma = \sigma_t + C d\epsilon^{el} = (\sigma_t + C d\epsilon) - C d\epsilon^{pl} = \sigma^{tr} - C d\epsilon^{pl} \tag{Eq 10}$$

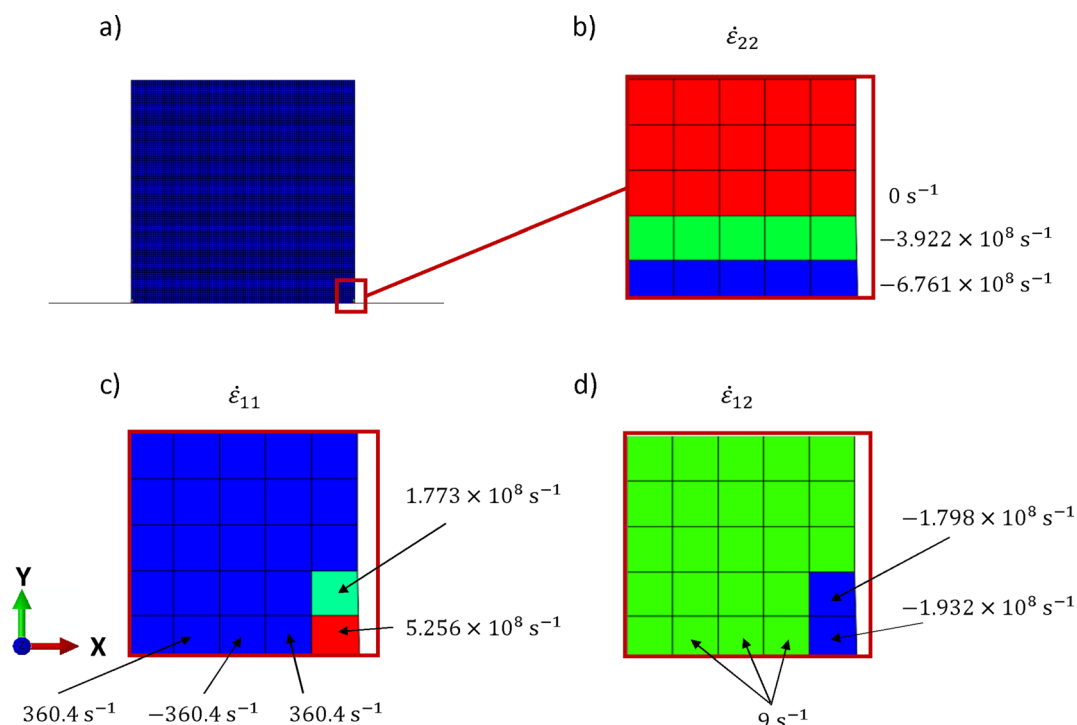


Fig. 10 Gradient of strain rate components, (a) The cuboid at 0.14 ns (or 140 ps) after the impact at 500 m/s, (b-d) are the enlargement of selected area in (a) showing respectively, strain rate components in x ($\dot{\epsilon}_{11}$), y ($\dot{\epsilon}_{22}$), and xy ($\dot{\epsilon}_{12}$) directions

Equation 9 and 10 reveal that once $d\epsilon^{pl}$ is determined, it becomes possible to calculate $d\epsilon^{el}$, and subsequently, the stress tensor can be computed. In continuum mechanics, the “consistency condition” (Ref 35) mandates the stress point to stay on or within the yield surface during plastic deformation, upholding the material’s physical behavior. Therefore, $d\epsilon^{pl}$ should be determined in a manner that aligns the calculated stress with the yield surface, leading to the term “ $Cd\epsilon^{pl}$ ” (in Eq 10) being referred to as the “Plastic corrector.” Correspondingly, $(\sigma_t + Cd\epsilon)$ is termed the “elastic predictor” (or trial stress, σ^{tr}).

For a von Mises material (Ref 34), typically employed for isotropic behavior, the consistency condition is defined as:

$$f = \sigma_e - \sigma_y = \sqrt{\frac{3}{2} \mathbf{S} : \mathbf{S}} - \sigma_y = 0 \quad (\text{Eq 11})$$

where σ_e represents the effective stress, a function derived from the deviatoric stress tensor, \mathbf{S} , while σ_y is the yield surface, which can be a function of plastic strain, strain rate and temperature. and can be influenced by factors such as plastic strain, strain rate, and temperature. Constitutive flow stress models, such as the JC model, are utilized within FEM to calculate the material’s yield surface, σ_y ,

during plastic deformation. It is apparent that f is less than zero during elastic deformation and should remain zero during plastic deformation.

An important point to note is that in FEM/Explicit, the consistency condition is applied at the beginning of each increment; however, it doesn’t guarantee its satisfaction at the end of the increment. As a result, there’s a potential for the solution to gradually deviate from the yield surface over multiple steps within the FEM/Explicit framework (Ref 14, 34-36). Consequently, ensuring small increment times in FEM/Explicit becomes necessary to minimize errors in the final calculated stresses.

The relationship between $d\epsilon^{pl}$ and the consistency condition, f , is established through the flow rule (Ref 14). According to this rule, the plastic strain increment occurs in a direction perpendicular to the tangent of the yield surface at the loading point, a concept known as the “normality hypothesis of plasticity” (Ref 39). Essentially, this implies that the maximum plastic strain increment arises where the maximum shear stress is present. As a result, the plastic strain increment and the total strain increment share the same direction because material deformation is initially assumed to be purely elastic. In essence, following the normality hypothesis of plasticity, the element experiencing the highest total strain increment

(i.e., the edge element) is also where the maximum plastic strain occurs.

For a von Mises material, the flow rule can be expressed as:

$$\dot{\epsilon}^p = \dot{\lambda} \frac{\partial f}{\partial \sigma} \text{ or } d\epsilon^p = d\lambda \frac{\partial f}{\partial \sigma} \tag{Eq 12}$$

where $\partial f / \partial \sigma$ is the direction of the plastic strain increment (or equivalently the plastic strain rate), and $\dot{\lambda}$ is called “plastic multiplier”. Substituting Eq (12) into Eq (11) yields:

$$d\epsilon^p = d\lambda \frac{3}{2} \frac{S}{\sigma_e} \tag{Eq 13}$$

Equation 13 elucidates that the determination of $d\lambda$ leads to the calculation of the plastic strain increment. An approximate method for calculating $d\lambda$ is as follows (Ref 40, 41):

$$d\lambda = \sqrt{\frac{3}{2}} \frac{\bar{\sigma}^{tr} - \sigma_y}{3\mu + h} \tag{Eq 14}$$

here, $\bar{\sigma}^{tr}$ signifies the equivalent trial stress (a known value), μ represents the shear modulus of the material, and $h = d\sigma_y / d\epsilon^{pl}$ denotes the rate of change of the flow stress model with respect to alterations in plastic deformation, termed “plastic hardening” (Ref 36, 41). This approximation remains valid particularly when the increment time in FEM/Explicit is exceedingly small.

By calculating the plastic multiplier, $d\lambda$, the increment in plastic strain can be determined, and consequently, the increment in stress can be established. At this stage, the total stress, strain, and temperature are updated for use at the beginning of the subsequent increment. Equation 14 emphasizes that the selection of the flow stress model exclusively influences the calculation of the plastic multiplier. The direction of the plastic strain, however, is determined by the elastic strain, remaining unaffected by the employed flow stress model.

The distribution of the equivalent plastic strain (PEEQ) and the plastic strain components at the edge of the cuboid at 0.3 ns is depicted in Fig. 11. The value of the plastic strain components is the cumulative sum of plastic strain increments from previous increments (increments 1 and 2 for this figure). It’s evident that the element at the tip of the cuboid’s edge exhibits the maximum PEEQ value, as shown in Fig. 11(a). The distribution of normal plastic strain in the x -direction (ϵ_{11}^{pl}), as illustrated in Fig. 11(c), and the shear plastic strain (ϵ_{12}^{pl}), shown in Fig. 11(d), follow a similar pattern to their corresponding total strain rate components displayed in Fig. 10. However, the distribution of normal plastic strain in the y -direction (ϵ_{22}^{pl}), presented in Fig. 11(b), exhibits slight differences from its

corresponding strain rate distribution. As evident, unlike the uniform strain rate distribution in the y -direction where all elements in each row displayed similar values, the plastic strain distribution in the y -direction exhibits higher values for the elements situated at the edges of the cuboid. This discrepancy can be attributed to the influence of equivalent strains (Fig. 11a) and stresses on the plastic multiplier and plastic strain, as elaborated in Eq 13 and 14. Consequently, the computed plastic strain for the element at the cuboid’s edge in the y -direction is higher compared to other elements in the same row due to experiencing elevated total strain and stress.

The distribution of normal stress in the x and y directions, shear stress, pressure, Mises stress, and Tresca stress along the edge of the cuboid is illustrated in Fig. 12(a) to (f), respectively. As shown, the normal stresses in both the x and y directions are not at their maximum at the element positioned at the tip of the cuboid’s edge. Nevertheless, it was demonstrated that this specific element undergoes the most significant stress increment during this particular time step. This inconsistency arises due to the use of ABAQUS/Explicit with the “true” or Cauchy stress tensor (Ref 14). Consequently, the values depicted in Fig. 12(a) and (b) encompass both hydrostatic and deviatoric stresses.

It is crucial to note that hydrostatic stress, also known as pressure (which is shown in Fig. 12d), solely influences the volume of the material or element, without inducing any shape alteration owing to the absence of shear components. Additionally, as previously discussed, the satisfaction of von Mises yield criterion (which is illustrated in Fig. 12e) is dependent solely on the deviatoric stress component, and it assumes the material’s plastic behavior to be incompressible. Therefore, plastic deformation remains unaffected by hydrostatic stress or pressure (Ref 35). In this context, the Tresca distribution (shown in Fig. 12f), illustrating the distribution of maximum shear stress, offers a more suitable method for identifying which element experiences the highest shear stress, directly corresponding to the maximum plastic strain.

Our exploration has revealed that regardless of the employed flow stress model and its incorporation of softening effects, the element positioned at the tip of the cuboid’s edge stands as the one experiencing the highest plastic strain. This insight is attributed to the specific boundary conditions applied to this particular element. This observation emphasizes that the outcomes generated by the flow stress model do not influence the fact that this specific element undergoes the most significant deformation compared to its counterparts. The flow stress model’s impact lies solely in determining the extent of this plastic deformation and the resulting plastic stress.

Figure 13 displays the temperature distribution along the edge of the cuboid at the 0.3 ns time point. In CS, material

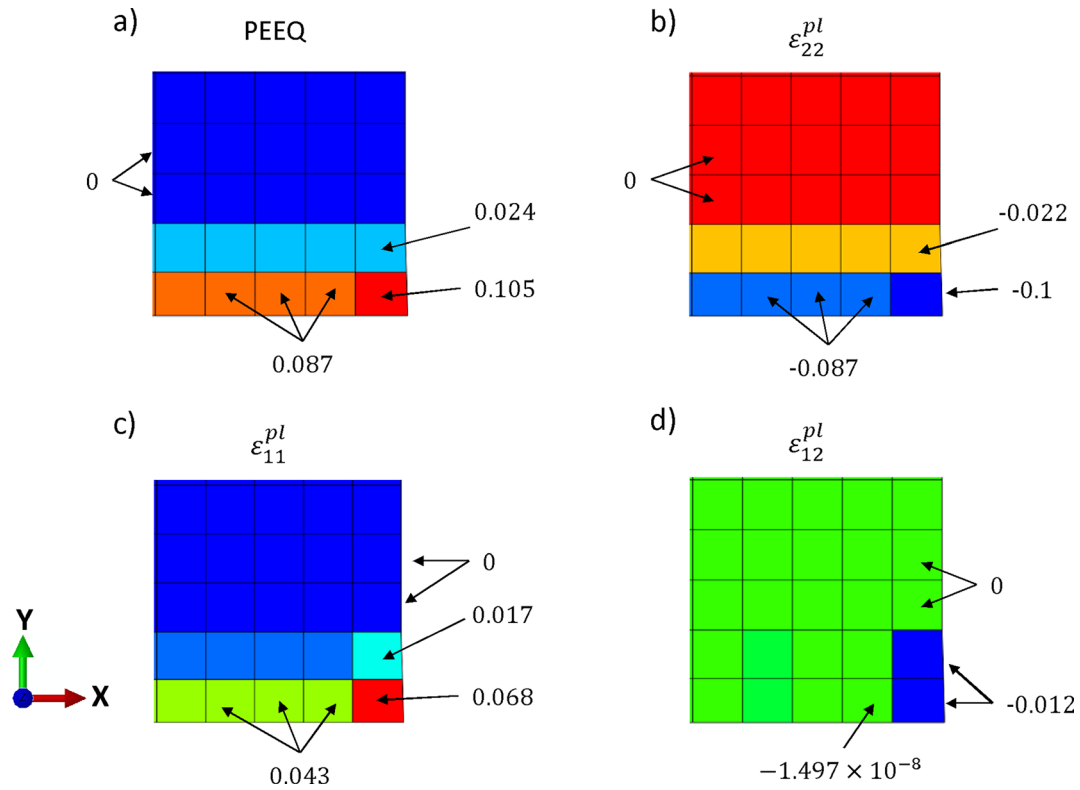


Fig. 11 Distribution of (a) equivalent plastic strain (or PEEQ), (b) normal plastic strain in *x*-direction, (c) normal plastic strain in *y*-direction, and (d) shear plastic strain at the edge of the cuboid at 0.3 ns

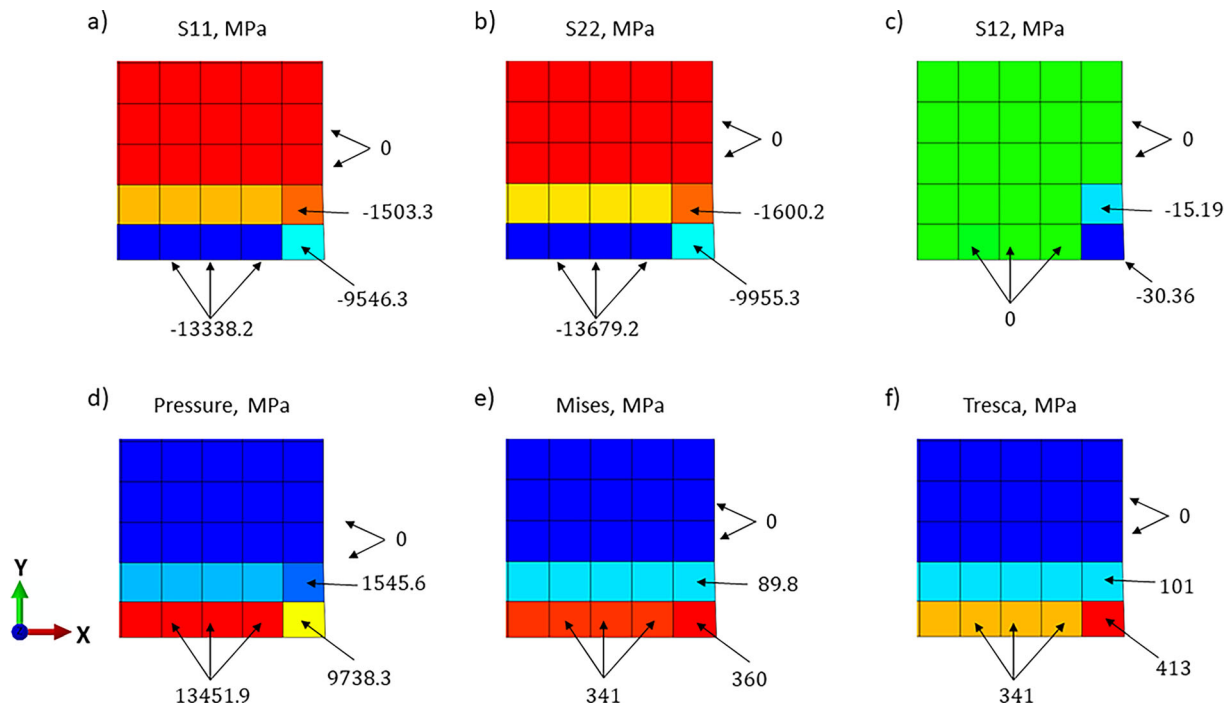


Fig. 12 Distribution of stress components—(a) Normal stress in the *x*-direction, (b) Normal stress in the *y*-direction, (c) Shear stress, (d) Pressure distribution, (e) Mises stress distribution, and (f) Tresca stress distribution at the edge of the cuboid at 0.3 ns

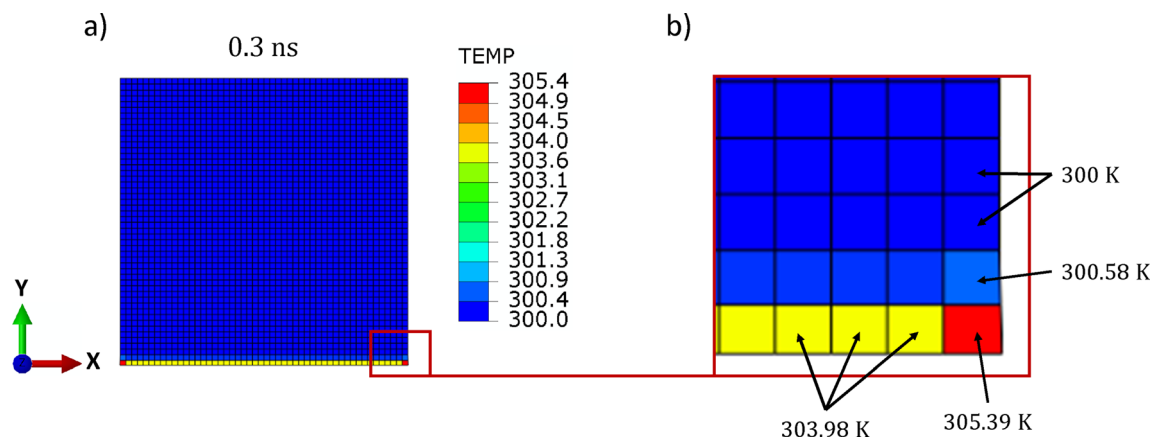


Fig. 13 (a) Temperature distribution on the cuboid at 0.3 ns (end of the second increment). (b) Enlarged view of the cuboid’s edge

deformation occurs within a very short time span, hence, it is assumed that there is negligible heat transfer within the material (Ref 42-48). Consequently, adiabatic analysis is usually employed in FEM/Explicit simulations of the CS process. In such an analysis, temperature does not serve as a degree of freedom in the simulation system. Instead, temperature increases are directly computed for each element, taking into account the level of plastic deformation and the stress experienced by that specific element. As depicted in Fig. 13, the element located at the tip of the cuboid’s edge exhibits the highest temperature, in line with its exposure to the maximum stress and strain. The calculation of the increment in temperature within FEM/Explicit follows this approach (Ref 14):

$$dT = \frac{\eta}{\rho C_p} \sigma : d\epsilon^{pl} \tag{Eq 15}$$

where dT denotes the incremental change in temperature at the end of the increment. Additionally, η represents the inelastic heat fraction, ρ stands for the material’s density, and C_p signifies the specific heat coefficient.

As deformation progresses, the element positioned at the tip of the cuboid’s edge consistently bears the highest applied shear stress, known as Tresca stress, when compared to all other elements. This phenomenon is a direct consequence of the specific boundary conditions assigned to the last node of this particular element, particularly the node on its right side. These conditions grant this node a greater degree of freedom in its movement to the right. This pattern endures until the element reaches a point of detachment from the underlying substrate. At this critical juncture, the shear stress experienced within the element undergoes a noticeable reduction. Following detachment, the neighboring element, still in contact with the substrate, takes the role of bearing the highest shear stress, as shown in Fig. 14.

Figure 14 displays snapshots of cuboid deformation at 5, 10, 15, and 20 ns, depicting Tresca stress distribution. Closer examination of the jetting area is provided in enlarged views at 10 and 20 ns, using different contour methods. Banded contours in the normal view images emphasize stress distribution, while quilt patterns in the enlargement view images highlight changes in Tresca stress during detachment. Figure 14 shows that the highest values of Tresca stress (or applied shear stress) consistently appears near the cuboid’s edge. As previously elucidated, this elevated shear stress in the edge region corresponds to the highest applied plastic strain. Consequently, it leads to the formation of jetting in this specific region, as visually demonstrated in Fig. 8. The enlargement view at 10 ns in Fig. 14 reveals detachment of the cuboid’s edge element, with the neighboring element bearing the maximum stress. Similarly, the second element also detaches and transfers its role to its neighbor to bear the maximum shear stress, see the enlargement view at 20 ns. This pattern persists as deformation continues, highlighting the dynamic nature of stress distribution during jetting formation.

In this section, the algorithm used by FEM/Explicit to calculate plastic deformation in high-velocity impact simulations was reviewed. The objective was to simplify the complexities of computational plasticity in continuum mechanics, making it more approachable. It was shown that the core concept behind FEM calculations is elegantly straightforward, however, its practical applications is vast and impactful. FEM stands as an impressive tool leveraged across diverse industries, including aerospace, automotive, marine, nuclear, and many others, owing to its inherent strength and versatility.

In the next section, we will discuss how initial assumptions and inputs affect the outcomes of the FEM and the conclusions that can be drawn from these results. We will highlight the importance of true validations,

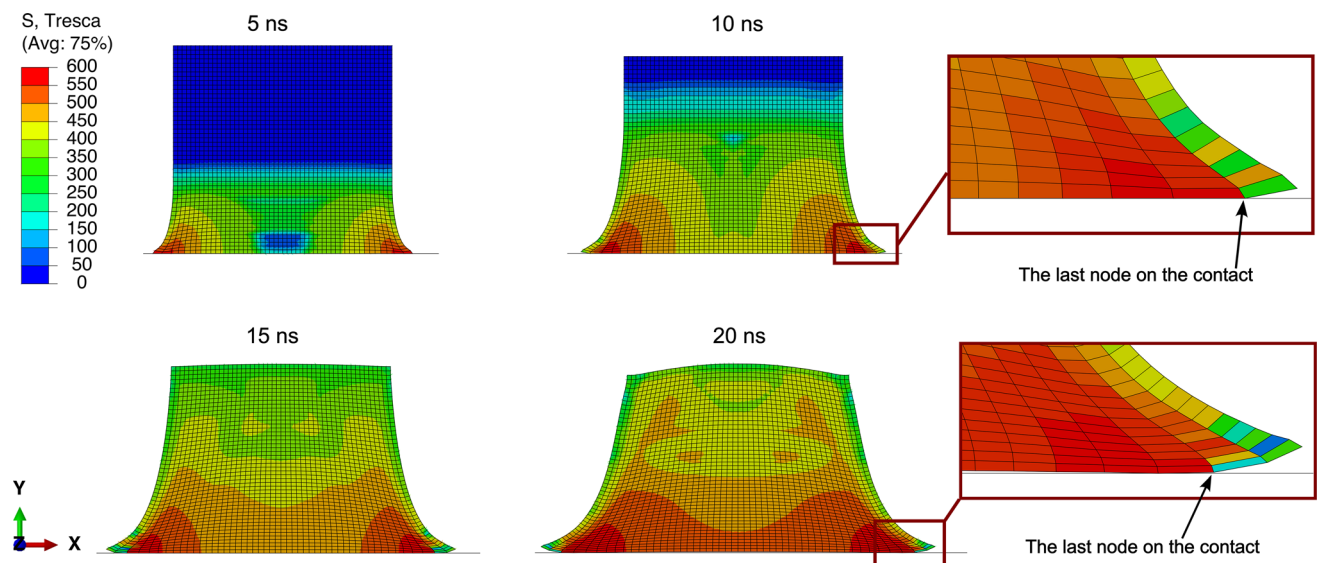


Fig. 14 Deformation snapshots and Tresca stress distribution during various time increments, with enlargement views highlighting jetting area. Banded contours are used for the normal view images,

emphasizing stress distribution, while quilt patterns are employed for the enlargement view images to highlight changes in Tresca stress during detachment

emphasizing that deriving accurate conclusions from the results is not possible without them.

Effect of Input Assumptions on FEM Conclusion

The accuracy of FEM results is highly dependent on how accurately the simulated process is defined. To achieve the most precise FEM results, the simulated process must be modeled as closely as possible to reality. Boundary conditions, degrees of freedom (DOF), loads, material properties, and material models are among the crucial factors influencing FEM outcomes. This section highlights the significance of flow stress model selection. The chosen flow stress model should comprehensively capture all material characteristics since FEM operates based on the provided equations. Therefore, it falls upon the user to employ valid equations and models that faithfully replicate the underlying physics of the process.

To emphasize the potential consequences of using an inaccurate flow stress model, a CEL simulation setup similar to the one used in (Ref 7) was employed. This setup involved simulating the impact of a 10 μm copper particle onto a copper substrate at a velocity of 550 m/s. Two simulations were carried out. In the first simulation, the softening component (the third bracket in Eq 1) of the JC model was excluded. In the second simulation, the hardening behavior was eliminated by setting $n = C = 0$ in the JC model (Eq 1). Consequently, the flow stress model in the first simulation cannot capture the softening behavior but only replicates the work hardening and strain rate hardening behaviors of the material. In the second

simulation, the flow stress model cannot represent the work and strain rate hardening but solely calculates the softening behavior of the material. The results are presented in Fig. 15(a) and (b).

As can be seen in Fig. 15, both simulations predicted jetting for both particle and the substrate at this velocity. As illustrated in the previous section, it was clarified that the direction of plastic deformation is linked to the applied boundary conditions, constraints, and the material's elastic behavior, rather than being dependent on the employed flow stress model. The chosen flow stress model only influences the extent of plastic deformation. This is evident in Fig. 15, where both simulations predicted jetting regardless of the different flow stress model; however, the second simulation (Fig. 15b) calculated a greater amount of jetting compared to the first simulation (Fig. 15a). Therefore, it is important to recognize that drawing conclusions solely based on the FEM results can be misleading. For instance, attributing jetting to thermal softening because the flow stress model accounted only for this effect (Fig. 15b) would be an oversimplification and may not accurately represent the real underlying mechanisms.

As demonstrated in this section, the outcomes of FEM simulations are a product of several influential factors, including the choice of constitutive flow stress model, material properties, boundary conditions, degree of freedoms, and more. Consequently, it is imperative for the user to possess a deep understanding of these contributing factors and their impact on simulation results. Furthermore, careful validation and verification of FEM predictions are essential steps in ensuring the accuracy and reliability of the simulation outcomes. This underscores the necessity for

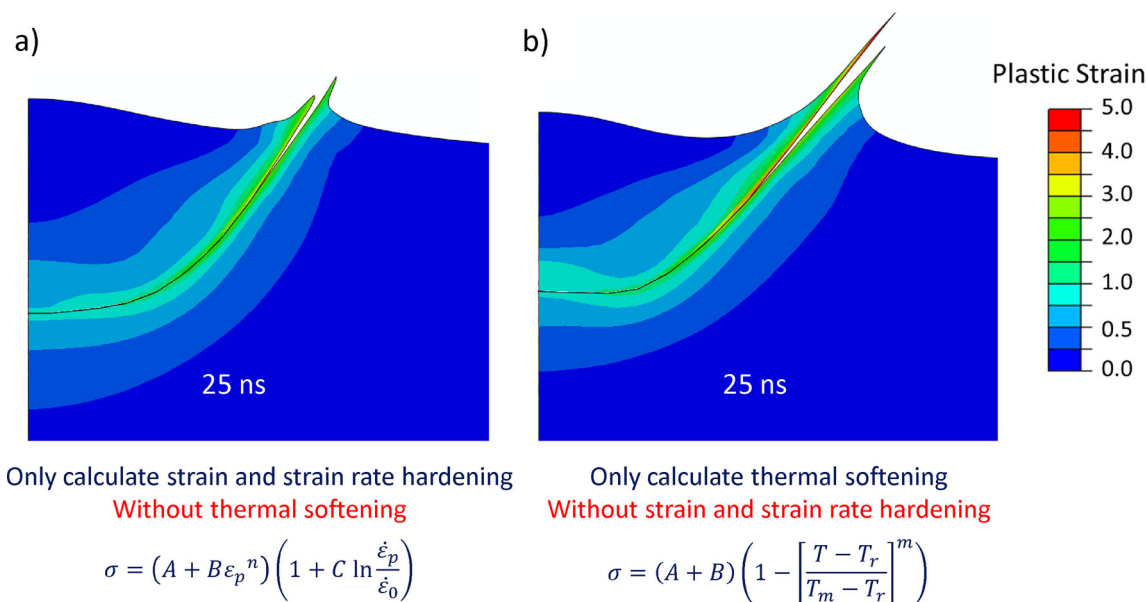


Fig. 15 Final deformed shape of a 10 μm copper particle impacting a copper substrate at 550 m/s. (a) Material without thermal softening capability, and (b) Material without strain and strain rate hardening capability

a comprehensive and attentive approach when utilizing FEM in simulations.

Summary

This work presented a concise critical review of two primary mechanisms proposed to explain jetting phenomenon in the context of CS. These mechanisms, known as Adiabatic Shear Instability (ASI) and Hydrodynamic Pressure-Release (HPR), originally found support primarily through FEM simulations. Our review not only highlights their pioneering work but also sheds light on the limitations of the methodologies used to establish these mechanisms.

Furthermore, this study reviewed the FEM/Explicit algorithm, emphasizing the factors influencing outcomes in FEM simulations. To clarify the procedure of plastic deformation calculation, the FEM’s formulas were examined in detail, using a case study of the impact of a cuboid against a rigid wall. Throughout this explanation, we aimed to simplify the complexities of FEM and its applications. Notably, it was highlighted that the choice of a flow stress model, such as the JC model, predominantly governs the magnitude of plastic deformation, while the direction of deformation is primarily determined by the applied boundary conditions, constraints, and the material’s elastic behavior.

This critical review aimed not only to provide valuable insights but also to indicate promising directions for future studies. While the FEM may lack the atomic-level resolution of MD, it excels in modeling single particle impacts

at the micrometer scale, which aligns with the conditions found in CS experiments. With precise material parameters, an accurate flow stress model, and a well-defined simulation setup, FEM emerges as a powerful computational technique for predicting the evolution of the deposition process in CS. We hope that this work will serve as an inspiration for researchers to refine and improve existing models, as well as to explore new and innovative methodologies for a deeper exploration of the material behavior and the mechanisms inherent in CS. A clearer understanding of the FEM algorithm could assist researchers in conducting FEM simulations more effectively, harnessing this powerful tool to enhance our comprehension in this complex field.

Appendix A: Cuboid Model

In the ABAQUS/Explicit software (Ref 14), a two-dimensional Lagrangian model employing four-node plane strain elements was employed to simulate the impact of a 50 μm copper cuboid onto a rigid wall (utilizing analytical rigid (Ref 14)). A mesh size of 1 μm was opted for to ensure accurate representation of the extensive deformation induced during high-velocity impacts. It’s worth noting that various element sizes were evaluated, and 1 μm was selected for its promising results in this study. A schematic representation of the simulation setup is shown in Fig. 16. The impact velocity was set at 500 m/s, and the initial temperature was maintained at room temperature (300 K). Outputs were saved for each increment to capture the

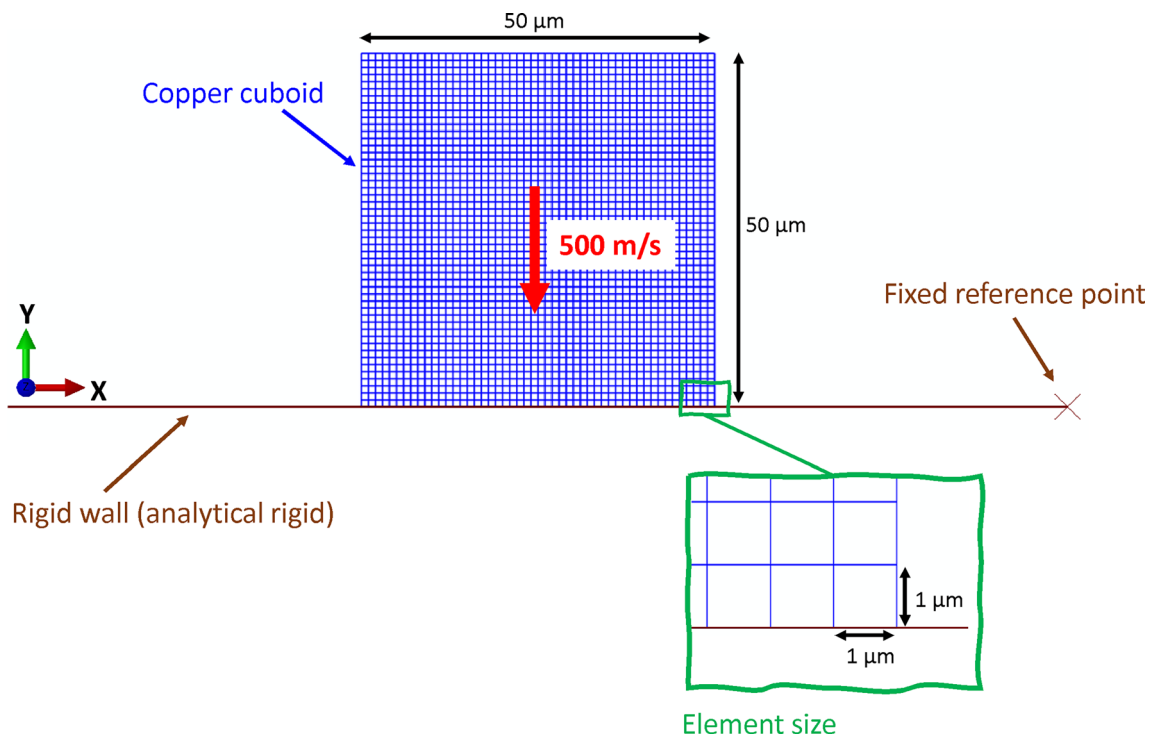


Fig. 16 Schematic representation of the simulation setup used in this study

Table 1 Material properties (Ref 10, 49)

Density, kg/m^3	8960
Specific heat, $\text{J}/(\text{kg K})$	383
Melting temperature, T_m , K	1357
Thermal conductivity, $\text{W}/(\text{m K})$	386
Inelastic heat fraction	0.9
Young's Modulus, GPa	124
Poisson's ratio	0.34
A , MPa	90
B , MPa	292
n	0.31
C	0.025
m	1.09
$\dot{\epsilon}_0$, s^{-1}	1
T_r , K	300

progressive behavior. For contact formulation, surface-to-surface contact was employed. The underside of the cuboid that collided with the substrate was defined as the slave surface (second surface), while the rigid wall surface was selected as the master surface (first surface) (Ref 14). The contact property was configured with a normal behavior (hard contact) using the default settings (Ref 14). Additionally, the material behavior was assumed to be linear

elastic in this simulation. The material properties utilized for this simulation are outlined in Table 1.

References

1. H. Assadi, H. Kreye, F. Gärtner, and T. Klassen, Cold Spraying—A Materials Perspective, *Acta Mater.*, 2016, **116**, p 382-407. <https://doi.org/10.1016/j.actamat.2016.06.034>
2. K. Kim, M. Watanabe, and S. Kuroda, Jetting-Out Phenomenon Associated with Bonding of Warm-Sprayed Titanium Particles onto Steel Substrate, *J. Therm. Spray Technol.*, 2009, **18**, p 490. <https://doi.org/10.1007/s11666-009-9379-1>
3. A.A. Tiarniyu, Y. Sun, K.A. Nelson, and C.A. Schuh, Site-Specific Study of Jetting, Bonding, and Local Deformation During High-Velocity Metallic Microparticle Impact, *Acta Mater.*, 2021, **202**, p 159-169. <https://doi.org/10.1016/j.actamat.2020.10.057>
4. M. Razavipour, S. Rahmati, A. Zúñiga, D. Criado, and B. Jodoin, Bonding Mechanisms in Cold Spray: Influence of Surface Oxidation During Powder Storage, *J. Therm. Spray Technol.*, 2020 <https://doi.org/10.1007/s11666-020-01123-5>
5. R. Nikbakht, M. Saadati, T.-S. Kim, M. Jahazi, H.S. Kim, and B. Jodoin, Cold Spray Deposition Characteristic and Bonding of CrMnCoFeNi High Entropy Alloy, *Surf. Coat. Technol.*, 2021, **425**, p 127748. <https://doi.org/10.1016/j.surfcoat.2021.127748>
6. H. Assadi, F. Gärtner, T. Stoltenhoff, and H. Kreye, Bonding Mechanism in Cold Gas Spraying, *Acta Mater.*, 2003, **51**, p 4379-4394. [https://doi.org/10.1016/S1359-6454\(03\)00274-X](https://doi.org/10.1016/S1359-6454(03)00274-X)
7. M. Hassani-Gangaraj, D. Veysset, V.K. Champagne, K.A. Nelson, and C.A. Schuh, Adiabatic Shear Instability is Not Necessary for Adhesion in Cold Spray, *Acta Mater.*, 2018, **158**, p 430-439. <https://doi.org/10.1016/j.actamat.2018.07.065>

8. H. Assadi, F. Gärtner, T. Klassen, and H. Kreye, Comment on ‘Adiabatic Shear Instability is Not Necessary for Adhesion in Cold Spray,’ *Scr. Mater.*, 2019, **162**, p 512-514. <https://doi.org/10.1016/j.scriptamat.2018.10.036>
9. M. Hassani-Gangaraj, D. Veysset, V.K. Champagne, K.A. Nelson, and C.A. Schuh, Response to Comment on “Adiabatic Shear Instability is Not Necessary for Adhesion in Cold Spray,” *Scr. Mater.*, 2019, **162**, p 515-519. <https://doi.org/10.1016/j.scriptamat.2018.12.015>
10. S. Rahmati and A. Ghaei, The Use of Particle/Substrate Material Models in Simulation of Cold-Gas Dynamic-Spray Process, *J. Therm. Spray Technol.*, 2014, **23**, p 530-540. <https://doi.org/10.1007/s11666-013-0051-4>
11. W.H. Johnson and G.R. Cook, A constitutive model and data for metals subjected to large strains, high strain rates and high. *Proceedings of the 7th International Symposium on Ballistics, The Hague, Netherlands* (1983), p. 541-547
12. C.Y. Gao and L.C. Zhang, A Constitutive Model for Dynamic Plasticity of FCC Metals, *Mater. Sci. Eng. A*, 2010, **527**, p 3138-3143. <https://doi.org/10.1016/j.msea.2010.01.083>
13. P. Landau, S. Osovski, A. Venkert, V. Gärtnerová, and D. Rittel, The Genesis of Adiabatic Shear Bands, *Sci. Rep.*, 2016, **6**, p 37226. <https://doi.org/10.1038/srep37226>
14. V. Abaqus, *6.14 Online Documentation Help Theory Manual: Dassault Systms*, Simulia Inc., Johnston, 2016.
15. M. Grujicic, C.L. Zhao, W.S. DeRosset, and D. Helfritch, Adiabatic Shear Instability Based Mechanism for Particles/Substrate Bonding in the Cold-Gas Dynamic-Spray Process, *Mater. Des.*, 2004, **25**, p 681-688. <https://doi.org/10.1016/j.matdes.2004.03.008>
16. G. Bae, Y. Xiong, S. Kumar, K. Kang, and C. Lee, General Aspects of Interface Bonding in Kinetic Sprayed Coatings, *Acta Mater.*, 2008, **56**, p 4858-4868. <https://doi.org/10.1016/J.ACTA MAT.2008.06.003>
17. C.J. Akisin, C.J. Bennett, F. Venturi, H. Assadi, and T. Hussain, Numerical and Experimental Analysis of the Deformation Behavior of CoCrFeNiMn High Entropy Alloy Particles onto Various Substrates During Cold Spraying, *J. Therm. Spray Technol.*, 2022, **31**, p 1085-1111. <https://doi.org/10.1007/s11666-022-01377-1>
18. Q. Chen, W. Xie, V.K. Champagne, A. Nardi, J.-H. Lee, and S. Müftü, On Adiabatic Shear Instability in Impacts of Micron-Scale Al-6061 Particles with Sapphire and Al-6061 Substrates, *Int. J. Plast.*, 2023, **166**, p 103630. <https://doi.org/10.1016/j.ijplas.2023.103630>
19. L. Palodhi and H. Singh, On the Dependence of Critical Velocity on the Material Properties During Cold Spray Process, *J. Therm. Spray Technol.*, 2020, **29**, p 1863-1875. <https://doi.org/10.1007/s11666-020-01105-7>
20. F. Meng, S. Yue, and J. Song, Quantitative Prediction of Critical Velocity and Deposition Efficiency in Cold-Spray: A Finite-Element Study, *Scr. Mater.*, 2015, **107**, p 83-87. <https://doi.org/10.1016/j.scriptamat.2015.05.026>
21. F. Meng, H. Aydin, S. Yue, and J. Song, The Effects of Contact Conditions on the Onset of Shear Instability in Cold-Spray, *J. Therm. Spray Technol.*, 2015, **24**, p 711-719. <https://doi.org/10.1007/s11666-015-0229-z>
22. C.-J. Li, W.-Y. Li, and H. Liao, Examination of the Critical Velocity for Deposition of Particles in Cold Spraying, *J. Therm. Spray Technol.*, 2006, **15**, p 212-222. <https://doi.org/10.1361/105996306X108093>
23. W.-Y. Li and W. Gao, Some Aspects on 3D Numerical Modeling of High Velocity Impact of Particles in Cold Spraying by Explicit Finite Element Analysis, *Appl. Surf. Sci.*, 2009, **255**, p 7878-7892. <https://doi.org/10.1016/J.APSUSC.2009.04.135>
24. W.-Y. Li, H. Liao, C.-J. Li, G. Li, C. Coddet, and X. Wang, On High Velocity Impact of Micro-Sized Metallic Particles in Cold Spraying, *Appl. Surf. Sci.*, 2006, **253**, p 2852. <https://doi.org/10.1016/j.apsusc.2006.05.126>
25. M.A. Adaan-Nyiaik and A.A. Tiamiyu, Recent Advances on Bonding Mechanism in Cold Spray Process: A Review of Single-Particle Impact Methods, *J. Mater. Res.*, 2023, **38**, p 69-95. <https://doi.org/10.1557/s43578-022-00764-2>
26. W.-Y. Li, S. Yin, and X.-F. Wang, Numerical Investigations of the Effect of Oblique Impact on Particle Deformation in Cold Spraying by the SPH Method, *Appl. Surf. Sci.*, 2010, **256**, p 3725-3734. <https://doi.org/10.1016/j.apsusc.2010.01.014>
27. M. Yu, W.-Y. Li, F.F. Wang, and H.L. Liao, Finite Element Simulation of Impacting Behavior of Particles in Cold Spraying by Eulerian Approach, *J. Therm. Spray Technol.*, 2012, **21**, p 745-752. <https://doi.org/10.1007/s11666-011-9717-y>
28. B. Yildirim, S. Muftu, and A. Gouldstone, Modeling of high velocity impact of spherical particles, *Wear*, 2011, **270**, p 703-713. <https://doi.org/10.1016/j.wear.2011.02.003>
29. S. Lepi, *Practical Guide to Finite Elements: A Solid Mechanics Approach*, Taylor & Francis, Oxford, 1998.
30. R. Hedayati and M. Sadighi, *Bird Strike: An Experimental Theoretical and Numerical Investigation*, Elsevier, Amsterdam, 2015.
31. K.H. Huebner, D.L. Dewhurst, D.E. Smith, and T.G. Byrom, *The Finite Element Method for Engineers*, Wiley, New York, 2001.
32. P. Wriggers, *Nonlinear Finite Element Methods*, Springer, Berlin Heidelberg, 2008.
33. L.M. Pereira, A. Zúñiga, B. Jodoin, R.G.A. Veiga, and S. Rahmati, Unraveling Jetting Mechanisms in High-Velocity Impact of Copper Particles Using Molecular Dynamics Simulations, *Addit. Manuf.*, 2023, **75**, p 103755. <https://doi.org/10.1016/j.addma.2023.103755>
34. F. Dunne and N. Petrinic, *Introduction to Computational Plasticity*, OUP Oxford, Oxford, 2005.
35. E.A. de Souza Neto, D. Peric, and D.R.J. Owen, *Computational Methods for Plasticity: Theory and Applications*, Wiley, New York, 2011.
36. A. Khoei, *Computational Plasticity in Powder Forming Processes*, Elsevier, Amsterdam, 2010.
37. Q.H. Shah and H. Abid, *LS-DYNA for Beginners: An Insight Into Ls-Prepost and Ls-Dyna*, LAP Lambert Academic Publishing, Saarbrücken, 2012.
38. L.M. Kachanov, *Fundamentals of the Theory of Plasticity*, Dover Publications, Mineola, 2013.
39. M. Okereke and S. Keates, *Finite Element Applications: A Practical Guide to the FEM Process*, Springer, Cham, 2018.
40. C.Y. Gao, FE Realization of a Thermo-Visco-Plastic Constitutive Model Using VUMAT in ABAQUS/Explicit Program. *Computational Mechanics: Proceedings of International Symposium on Computational Mechanics* (Springer, Berlin, Heidelberg, 2009), p. 301
41. L. Ming and O. Pantalé, An Efficient and Robust VUMAT Implementation of Elastoplastic Constitutive Laws in Abaqus/Explicit Finite Element Code, *Mech. Ind.*, 2018, **19**, p 308. <https://doi.org/10.1051/meca/2018021>
42. G.N. Devi, S. Kumar, T.B. Mangalarapu, G. Vinay, N.M. Chavan, and A.V. Gopal, Assessing Critical Process Condition for Bonding in Cold Spraying, *Surf. Coat. Technol.*, 2023, **470**, p 129839. <https://doi.org/10.1016/j.surfcoat.2023.129839>

43. Z. Dai, F. Xu, J. Wang, and L. Wang, Investigation of Dynamic Contact Between Cold Spray Particles and Substrate Based on 2D SPH Method, *Int. J. Solids Struct.*, 2023, **284**, p 112520. <https://doi.org/10.1016/j.ijsolstr.2023.112520>
44. S. Rahmati, A. Zúñiga, B. Jodoin, and R.G.A. Veiga, Deformation of Copper Particles Upon Impact: A Molecular Dynamics Study of Cold Spray, *Comput. Mater. Sci.*, 2020, **171**, p 109219. <https://doi.org/10.1016/j.commatsci.2019.109219>
45. N. Deng, D. Qu, K. Zhang, G. Liu, S. Li, and Z. Zhou, Simulation and Experimental Study on Cold Sprayed WCu Composite with High Retainability of W Using Core-Shell Powder, *Surf. Coat. Technol.*, 2023, **466**, p 129639. <https://doi.org/10.1016/j.surfcoat.2023.129639>
46. P. Khamsepour, C. Moreau, and A. Dolatabadi, Effect of Particle and Substrate Pre-heating on the Oxide Layer and Material Jet Formation in Solid-State Spray Deposition: A Numerical Study, *J. Therm. Spray Technol.*, 2023, **32**, p 1153-1166. <https://doi.org/10.1007/s11666-022-01509-7>
47. S. Rahmati and B. Jodoin, Physically Based Finite Element Modeling Method to Predict Metallic Bonding in Cold Spray, *J. Therm. Spray Technol.*, 2020, **29**, p 611-629. <https://doi.org/10.1007/s11666-020-01000-1>
48. S. Rahmati, R.G.A. Veiga, A. Zúñiga, and B. Jodoin, A Numerical Approach to Study the Oxide Layer Effect on Adhesion in Cold Spray, *J. Therm. Spray Technol.*, 2021 <https://doi.org/10.1007/s11666-021-01245-4>
49. W.Y. Li, C. Zhang, C.-J. Li, and H. Liao, Modeling Aspects of High Velocity Impact of Particles in Cold Spraying by Explicit Finite Element Analysis, *ASM Int.*, 2009, **18**, p 921-933.

Publisher's Note Springer Nature remains neutral with regard to jurisdictional claims in published maps and institutional affiliations.

Springer Nature or its licensor (e.g. a society or other partner) holds exclusive rights to this article under a publishing agreement with the author(s) or other rightsholder(s); author self-archiving of the accepted manuscript version of this article is solely governed by the terms of such publishing agreement and applicable law.